Geomech. Geophys. Geo-energ. Geo-resour. (2023) 9:169
https://doi.org/10.1007/s40948-023-00711-3

RESEARCH

Thermal damage evolution of granite under different thermal conditions based on two-scale tessellation via discrete element method

Qianchi Ma · Xiaoli Liu · Danqing Song · Enzhi Wang · Jianmin Zhang · Wenli Yao · Mingyang Wang

Received: 2 August 2023 / Accepted: 29 November 2023

Abstract This paper presents a numerical modeling method that integrates a grain-growth model and Voronoi polygon configuration to investigate the thermal damage characteristics and fracture mechanism of granite under three distinct thermal conditions: rapid heating, slow heating, and cycle heating. The proposed method accurately simulates the intra-grain damage modes of mineral particles and the mechanical responses of granite. Through the simulation, it was observed that slow heating induces more significant deterioration compared to rapid heating, while cycle heating leads to wider crack openings and apparent brittle damage during the cooling phase. Furthermore, the peak strength and elastic modulus of granite demonstrate a significant decrease with increasing temperature under all three heating conditions. Notably, slow heating exhibits ductility characteristics in its post-peak residual strength. This study also analyzes the effects of different thermal conditions on the damage evolution pattern and cracking mechanism of rocks. It is found that slow heating generates a higher number of cracks with a broader distribution and intra-grain damage, whereas cycle heating results in severe cracks and fractures. The findings of this study have practical implications for preventing and controlling thermal disasters in deep rock engineering.

Article highlights

(1) Developed 3DEC-GBM model integrating Grain-Growth and Voronoi for intra/transgranular behavior.
(2) Conducted thermomechanical calculations considering mineral heterogeneity.
(3) Compared crack development and macro-mechanical parameters under three heating conditions.

Keywords Thermal damage evolution · Granite · Different thermal conditions · two-scale tessellation · Discrete element method

1 Introduction

With the rapid global development, the demand for the development of deep rock masses has significantly increased. Various large-scale rock projects, such as deeply buried underground oil storage reservoirs, deep burial of nuclear waste containment, deep oil extraction wells, and deep subway pipelines, have been designed to meet these demands (Bérest and Brouard 2003; Gautam et al. 2021; Kochkin et al. 2021; Chen et al. 2021). However, these projects are

Q. Ma · X. Liu (✉) · D. Song · E. Wang · J. Zhang · W. Yao · M. Wang
State Key Laboratory of Hydroscience and Engineering, Tsinghua University, Beijing 100084, China
e-mail: xiaoli.liu@tsinghua.edu.cn

Published online: 14 December 2023

often exposed to the effects of high temperatures, leading to thermal hazards in deep subsurface spaces. These hazards pose significant challenges for construction, operation, and engineering maintenance in deep subsurface spaces, resulting in adverse effects. Figure 1 presents photographs depicting an underground coal mine fire in India (Tripathi et al. 2021), highlighting the importance of studying thermal hazards in deep rock masses. Therefore, the study of thermal hazards in deep rock masses is significant and has become one of the hot issues in the field of rock mechanics. In closed or abandoned mines, the presence of remaining coal mines can pose a risk of fire. The deeper sections of these abandoned mines are typically surrounded by granite. To ensure the safety and stability of these mines, it is crucial to conduct comprehensive research on the damage and fracture mechanism of the granite surrounding rocks under high temperatures. Understanding the properties and behavior of granite host rocks in high-temperature environments is essential for preventing potential fires and preserving the integrity of mine structures. Such research can offer valuable insights to develop effective safety measures and maintenance strategies.

Granite, characterized by its non-uniform composition, primarily consists of minerals such as quartz, feldspar, biotite, and others. At room temperature, granite exhibits good stability and rock strength. However, when subjected to high temperatures, the strength of granite undergoes a significant decrease (Kumari et al. 2019; Qin et al. 2020). This phenomenon can be attributed to the impact of temperature on the inter-particle strength within the rock, as well as the varying coefficients of thermal expansion among different minerals, which affect the volume expansion of each mineral. As a result, the non-uniform expansion of granite upon heating generates thermal stresses within the rock, leading to the initiation of microcracks and alterations in the rock's microstructure (Johnson et al. 1978; Zuo et al. 2017). Moreover, thermal stresses can cause the rupture of mineral grains, resulting in crack formation. Understanding the effect of granite's non-uniformity after heating on thermal damage and analyzing the thermal damage mechanism and mechanical response characteristics of granite are of great significance for the development of deep rock engineering and ensuring the stable operation of projects.

Rock thermal damage has garnered significant attention from scholars (Lei et al. 2019; Srinivasan et al. 2020; Yang et al. 2019), and indoor rock mechanics tests and numerical simulations have emerged as the primary methods for studying this phenomenon. Indoor rock mechanics tests enable in situ sampling and offer a more accurate representation of rock conditions at project sites. Huang et al. (2022) conducted dynamic mechanical response tests on fractured water-filled granite using the Split Hopkinson Pressure Bar (SHPB) technique in a laboratory. Du et al. (2020) studied the dynamic loading mechanics of sandstone cycles around open pit mines through indoor tests. Wang and Cai (2019) performed heating tests on granite and found that the final heating temperature significantly affected the uniaxial compression strength, while the heating rate did not. Ghasemi et al. (2020) observed the

Fig. 1 Geological hazards caused by underground coal mine fires in India: **a** Obvious cracks and subsidence with coal fires underground; **b** Land disturbance with visible coal fires spewing flames (Tripathi et al. 2021)

microstructure of rocks after heating, analyzing the role of various minerals in thermal damage. Luc Leroy et al. (2021) investigated high-temperature tests on granite, sandstone, and mudstone, concluding that high temperatures reduce the mechanical properties of rocks by over 75%. Ersoy et al. (2019) compared the strength changes of rocks after high-temperature heating under different cooling methods and fitted a predictable curve for rock damage strength after exposure to high temperatures. Freire-Lista et al. (2016) subjected granite to cycle heating and observed the microcracks produced using petrography and fluorescence microscopy. However, indoor rock mechanics tests have certain limitations, such as the discrete nature of rock specimens leading to significant test result dispersion. Therefore, it is necessary to observe the rock microstructure after the tests using techniques like electron microscopy. To address these limitations, scholars have turned to numerical simulation studies. For example, Zhao et al. (2022) used the PFC2D (Particle Flow Code in 2 Dimensions) method to investigate the effect of ultrasonic vibration on rock damage at high temperatures. Wang and Konietzky (2020) employed finite-difference simulations to evaluate differences in granite thermal damage under slow and rapid heating conditions. Vogler et al. (2020) conducted numerical simulations to study the damage process on the rock surface under rapid heating, exploring the impact of maximum heating rate and temperature. Wu et al. (2020) developed a model of prefabricated cracks and examined the Brazilian disc test after heating, demonstrating that the strength of the Brazilian disc test decreased with increased fracture pore size. Toifl et al. (2017) used a finite element method combined with a Voronoi polygon to explore the simulation results of electromagnetic fields on microwave radiation of granite. Numerical simulations offer advantages such as low cost, accurate simulation, and good repeatability. They can simulate complex physical conditions, significantly reducing research costs and mitigating risks for testers. Furthermore, numerical simulations can depict microscopic fractures within rocks, providing a more comprehensive and intuitive understanding of internal structural damage.

In previous studies, experimental investigations on rocks have primarily focused on changes in physical properties after heat treatment, including variations in wave velocity, volume, and mass. Mechanical tests have also been conducted on heat-treated specimens to compare the changes in mechanical strength before and after heating. However, these tests often lack standardized procedures, with variations among individual rock specimens, and insufficient documentation of the entire testing process. Furthermore, there have been limited numerical simulations of rock heating, which typically focus on studying the cracking behavior of thermally-induced fractures, while comprehensive thermal coupling studies are lacking.

In the context of rock engineering or geological issues, traditional numerical methods such as the finite element method (FEM) and finite difference method (FDM) may prove ineffective in simulating complex geological effects. Moreover, the results obtained from FEM and FDM simulations may exhibit significant deviations after the calculations are completed. However, the discrete element method (DEM) simulation method offers distinct advantages for modeling the mechanical behavior of rock structures. DEM allows for the specification of simulation problems based on specific data, rather than relying on complex geometric and physical parameters (Jing and Stephansson 2007). DEM offers several specific advantages. First, it allows for faster calculation of complex components and their interactions, enabling more efficient analysis of volatility and reflections (Elmo et al. 2013). Second, DEM is well-suited for modeling various physical phenomena, including hydrodynamics, gravitational acceleration, and energy changes. Finally, DEM is particularly suitable for simulating problems related to porous media, such as vegetation, earthquakes, and minerals.

In this study, the focus is on investigating the thermal damage characteristics of granite using the discrete element method (DEM) and integrating a two-scale modeling approach. The goal is to refine the fracture description method for rock rupture and achieve thermal coupling calculations under different heating methods. To begin, the model incorporates various contact parameters to accurately simulate the mechanical behavior of the rock, aligning the simulation results with the outcomes of mechanical tests. This ensures that the model can effectively represent the rock's response to different loading conditions. Next, by considering mechanical indicators such as peak strength, elastic modulus, and residual strength,

the study aims to assess the extent of thermal damage incurred by the rock during the thermal coupling process. The qualitative and quantitative description methods employed in the analysis enable the demonstration of both internal and external factors contributing to rock thermal damage. This comprehensive approach provides a closer representation of the realistic performance of post-thermal cracking in rocks and offers valuable insights into the behavior of high-temperature rocks. In summary, this study combines the discrete element method, a two-scale modeling approach, and refined fracture description methods to investigate the thermal damage characteristics of granite. The analysis includes mechanical test validation, qualitative and quantitative assessments of thermal damage, and an examination of the internal and external causes of rock damage. The findings of this study can provide valuable references for understanding the behavior of high-temperature rocks and their response to thermal loading.

2 Modeling and thermodynamic coupling simulation method

2.1 Voronoi tesselation and Laguerre tesselation

Tessellation, also known as tiling, involves filling a three-dimensional spatial domain with repeated patterns or cells while ensuring there are no gaps or overlapping spaces. Voronoi tessellation, a spatial analysis method based on a set of data points, partitions the space into multiple regions. Each region, called a Voronoi cell, is defined by polygons formed using the data points as vertices. This method guarantees that every point within a region is closer to a specific data point than to any other point, facilitating accurate spatial separation. Voronoi tessellation finds extensive applications in diverse fields such as geographic information systems, computer graphics, and materials science.

Laguerre tessellation is another spatial analysis technique that divides space into convex polyhedral regions. It employs Laguerre balls centered on data points, with each Laguerre cell defined as the intersection of all Laguerre balls containing a given point. Laguerre tessellation is widely utilized in computer graphics, spatial statistics, and pattern recognition.

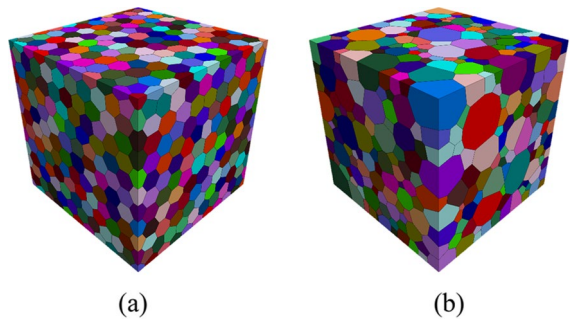

Fig. 2 Comparison of Voronoi tessellation and Laguerre tessellation. **a** shows a cube composed of Voronoi cells as presented in the official example of 3DEC. In the 10×10×10 cube, a total of 1499 blocks are present. **b** shows the same 1499 blocks in a 10×10×10 cube generated by the grain-growth model in Neper

In the context of 3DEC, a software tool, the generation of Voronoi blocks follows a specific geometric approach, typically using a cube, and the average edge length is set by the user. Voronoi blocks are created within the designated object using the block create command. The primary criteria for Voronoi block generation in 3DEC rely on the specified edge length. As shown in Fig. 2a, the blocks in the model are quite similar in terms of both shape and size, and the exact number of Voronoi blocks within the object cannot be explicitly specified.The Voronoi tessellation mothed defined as follows, being given a spatial domain $D \in \mathfrak{R}^n$ and a set of seeds $\{S_i(x_i, w_i), i = 1, \cdots, N\}$, each seed, S_i is defined by its coordinates, x_i, Every seed S_i is associated with a Voronoi cell C_i as follows,

$$C_i = \{P(x) \in D | d_E(P, S_i) < d_E(P, S_j) \forall j \neq i\}$$

where d_E is the Euclidean distance.

The Laguerre tessellation analytical is defined as follows, being given a spatial domain $D \in \mathfrak{R}^n$ and a set of seeds $\{S_i(x_i, w_i), i = 1, \cdots, N\}$, each seed, S_i is defined by its coordinates, x_i, and a non-negative weight, w_i. Every seed S_i is associated with a Laguerre cell C_i as follows,

$$C_i = \{P(x) \in D | d_L(P, S_i) < d_L(P, S_j) \forall j \neq i\}$$
$$\text{with} d_L(P, S.) = d_E(P, S.)^2 - w.$$

where, d_L referred to as power distance and d_E is the Euclidean distance. Since the Euclidean distance is

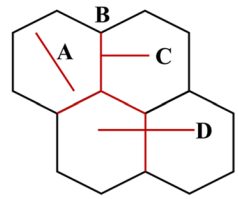

Fig. 3 Possible fracture patterns during rock destruction: **A** denote for cracks intra-grains; **B** denote for cracks inter-grains; **C** denote for the cracks start with inter-grains; **D** denote for cracks cross grains (Ghasemi et al. 2020)

defined with the coordinates, the power distance is mainly associated with the seed's weight.

Neper is an open-source software that is primarily used for generating complex microstructures based on specific design criteria (Quey et al. 2011, 2018; Quey and Renversade 2018). It offers a diverse range of functionalities that enable the creation of models at various scales, making it possible to simulate intricate materials and structures. Additionally, Neper's computational capabilities allow for the optimization of these models, ensuring improved performance and efficiency.

The grain-growth model implemented in Neper is based on Laguerre tessellation, which provides a topological representation of a polycrystal composed of grain boundaries, triple junctions, and quadruple points. In comparison to Voronoi tessellation, Laguerre tessellation offers the advantage of describing any normal tessellation, irrespective of cell shape or arrangement. As shown in Fig. 2b, unlike Voronoi cells, Laguerre cells can exhibit variations in cell size, and their geometries are not limited by the equidistant nature of the faces in Voronoi cells. Consequently, Laguerre tessellation is considered both general and optimal for tessellations composed of convex cells.

In the context of representing rocks, Laguerre tessellation is considered more suitable than Voronoi tessellation. This is because Laguerre tessellation has the ability to account for the roundness and size distribution of granular particles, which are typically found in rocks. Unlike Voronoi tessellation, Laguerre tessellation provides a more accurate representation of the structure of rocks that consist of mineral particles with diverse shapes. Voronoi tessellation may encounter computational issues related to singular points and boundary points, whereas Laguerre tessellation, with its spherical structure, is better equipped to handle such situations. Furthermore, Laguerre tessellation allows for the generation of structures through 2D planar projections and 3D spherical cuts, which reduces the computational complexity involved in generating 3D structures compared to Voronoi tessellation.

2.2 Two-scale tessellation in Neper

The Voronoi polygon rule is a mathematically based geometric method that connects the midpoints of the sides of a polygon. The triangular division method, often resulting in relatively smooth sections of damage, is more suitable for simulating shear damage. On the other hand, the Voronoi polygon damage approach better represents the failure mode of rocks (Ghazvinian et al. 2014).

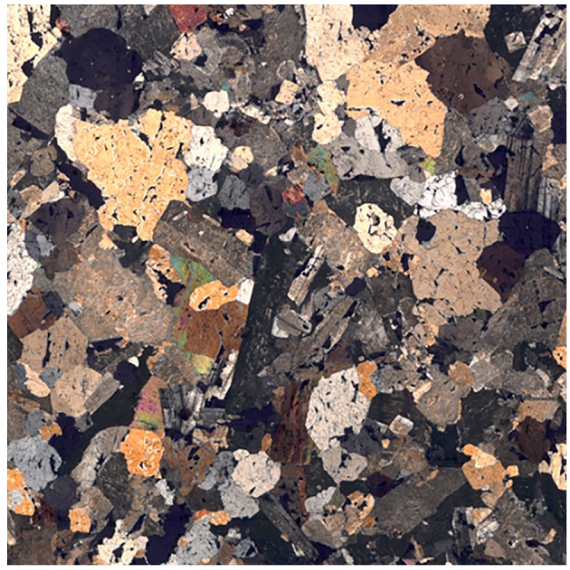

Fig. 4 Mineral composition of granite. Microstructure image of granite (Wang and Konietzky 2020)

Table 1 Micro-material properties of granite (Li et al. 2019)

	Proportion (%)	Density (kg/m^3)	Young's modulus (GPa)	Poisson's ratio	Thermal expansion coefficient (k^{-1})	Thermal conductivity (W/(m·k))	Specific heat (J/(kg·K))
Quartz	30	2650	95	0.07	1.21×10^{-5}	6.5	730
Feldspar	60	2600	78	0.33	3.6×10^{-6}	2.15	640
Biotite	10	3000	39	0.2	1.11×10^{-5}	5.25	600

This geometric computational model has been implemented in several computational software packages. In this study, a two-scale model configuration approach is utilized to simulate both intra-grain damage within the granite and the destruction of the crystals themselves. Figure 3 illustrates the potential rupture pattern between crystals. In traditional block discrete element approaches, the blocks do not undergo damage, making it challenging to simulate intra-grain damage in tests. The Voronoi polygon generated in the simulation software exhibits an approximate hexagonal shape and relatively similar sizes. Granite is an inhomogeneous rock concerning both mineral composition and grain size. The model generated using this method in our study can accurately reflect the geological structure of granite. The proportions of the three main minerals in typical granite are very similar. Quartz minerals account for approximately 25%-30%, feldspar minerals account for about 60%, biotite minerals account for less than 10%, and other minerals account for less than 2% (Li et al. 2019, 2022; Shang et al. 2019). In this study, we adopted a ratio of 30% quartz, 60% feldspar, and 10% biotite. Figure 4 presents a schematic diagram of the microstructure of multiple minerals in granite and the proportions of component minerals (Table 1).

This study utilizes Neper to generate a two-scale model with the aim of overcoming the restrictions posed by discrete elements of the block. This enables the block itself to be destructed again, thereby demonstrating the transgranular damage of the model mineral particles. To utilize a two-scale model in neper, it is essential to establish the number of levels for each scale. The first level indicates the quantity of mineral units present in the model, while the second level determines the subdivision of each mineral into smaller units. In this study, the first layer of modeling rules is based on the grain-growth model, which is applicable to crystalline materials (Frost and Thompson 1996). As granite is a crystalline rock, this model is suitable for representing it. The second layer of rules continues to utilize the Voronoi polygon rule. The division number of the first layer is denoted as M, while the division number of the second layer is denoted as N, resulting in the model being denoted as M×N. The model dimensions are 50 mm in diameter and 100 mm in height. Figure 5 provides a schematic diagram of the model, comprising 2000×6 divisions, generated using the Neper software. Each small unit within the model has a minimum diameter of 1 mm, ensuring a higher level of realism and closely resembling granite. However, the computational efficiency of this model is considerably low, primarily due to the limitations of the discrete element software that employs Newton's second law (F = ma) to compute physical quantities such as block velocity and displacement (Itasca Consulting Group 2019).

After conducting multiple tests and considering computational limitations, it was found that using a

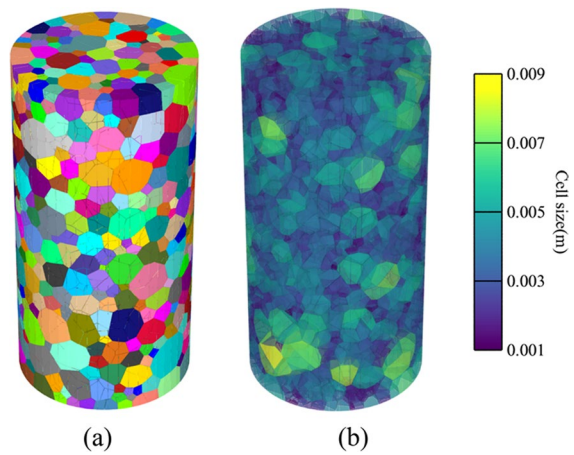

Fig. 5 Two-scale tessellation in Neper for 2000×6 **a** Grouping diagram of granite models in Neper; **b** Mineral particle size map by Neper statistics

large number of blocks (more than 2000) leads to an enormous matrix and requires several days to complete calculations. However, if the number of blocks is less than 50, the representation of inter-grain and intra-grain damage becomes inadequate, even though the calculations can be completed quickly. It is acknowledged that increasing the number of units improves the accuracy of describing thermal damage in rocks. Nevertheless, the three-dimensional 3DEC thermal coupling calculation suffers from slow calculation efficiency. Taking into account the limitations of computer computing power, the author conducted a series of tests and selected the 30X4 model, the random distribution of properties (RDP) method was used to define each group as different mineral properties. This model ensures non-uniformity of the model while better restoring the mechanical strength of granite and describing damage between and within particles. It should be noted that, from a mineralogical perspective, the particle size in this study is relatively large.

2.3 Parameters setting

The primary purpose of the mechanical parameter setting is to perform accurate simulation calculations of the contact to obtain simulation results consistent with the rock mechanics test. The parameter setting mainly has the following parameters to be set, namely: JK_n, JK_s, JK_n/JK_s, JC_m, $J\phi_m$, $J\sigma_{tm}$, JC_r, $J\phi_r$, $J\sigma_{tr}$. Where JK_n And JKs denote normal and shear stiffness of grain contact, respectively; JC_m and JC_r denote cohesion of contact with Mohr–Coulomb and residual, respectively; $J\phi_m$ and $J\phi_r$ denote friction angles of and contact with Mohr–Coulomb and residual, respectively; $J\sigma_{tm}$ and $J\sigma_{tr}$ denote tensile strength of and contact with Mohr–Coulomb and residual, respectively. Regarding the mechanical calculation part, the flow chart for setting the GBM parameters of 3DEC is shown in Fig. 6.

There are two main parts to the setting of mechanical parameters. Firstly, the adjustment of deformation parameters. The Poisson's ratio is only positively related to JK_n/JK_s. The value of JK_n is fixed, and the ratio of JK_n/JK_s is adjusted to satisfy the Poisson's ratio of the rock. The next step is to adjust the modulus of elasticity, which is still

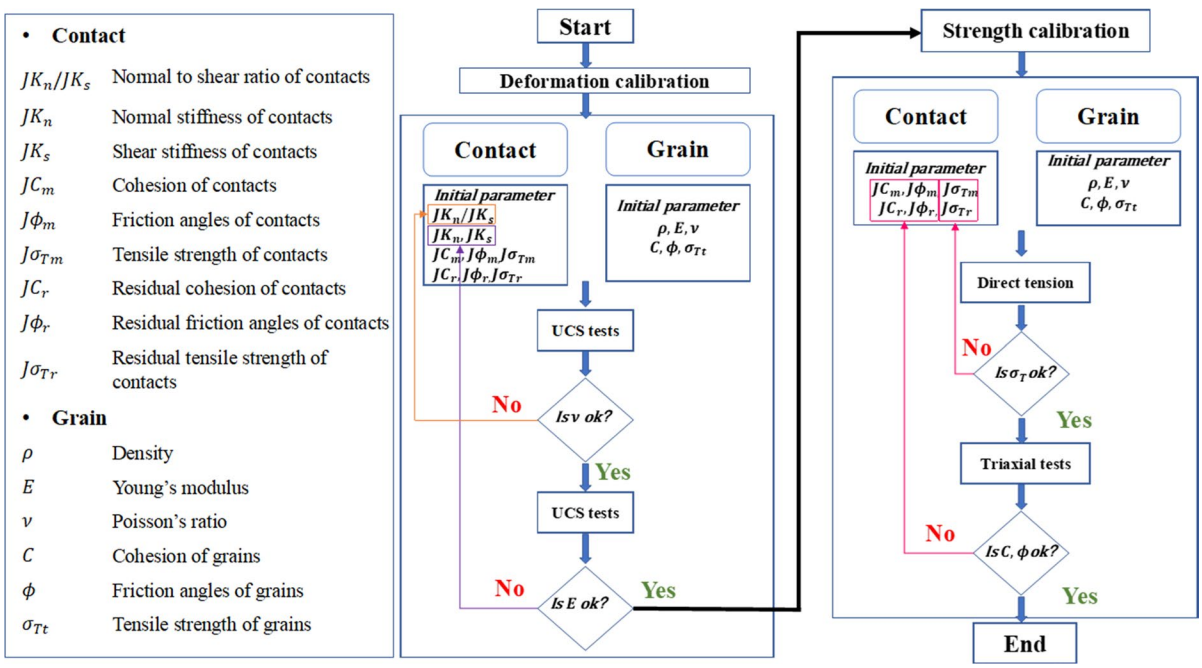

Fig. 6 Process for parameter setting for 3DEC-GBMs (modified from Wang and Cai 2019)

adjusted with the UCS simulation. The magnitude of the elastic modulus is positively proportional to the value of JK_n, and the result of the calculation is adjusted by adjusting the magnitude of JK_n until it satisfies the elastic modulus of the rock (Wang and Cai 2018, 2019). The second part is the mechanical parameters, mainly the adjustment of tensile strength and cohesion friction angle. The simulation of tensile strength is proportional to the tensile strength parameter, and the cohesion and friction angle is determined by using direct tension simulation and triaxial compression and plotting the envelope, respectively. A series of adjustments were made to enable the simulation results to meet the experimental results. The results of experimental data from previous studies were selected (Yujie et al. 2020), as shown in Table 2. After parameter setting, nine types of contact were used in this study, and the specific values are shown in Table 3. After testing, combined with the results of previous studies, the residual strengths were all obtained as constant values. The parameter adjustment process for heterogeneous models is relatively more complex. Currently, the most recognized method is to adjust the parameters of each mineral individually until it meets the experimentally measured mechanical performance indicators. The average value of the two minerals is then taken at the contact where they touch each other. Regarding the contact parameters within minerals, there have been limited studies conducted thus far. Previous studies have commonly used values that establish larger internal contact parameters compared to the contact parameters between particles. In this study, we have referred to previous research and set the contact parameters inside the particles to be 1.5 times the basic parameters between particles (Wang and Cai 2018).

Table 2 Comparison test selected for parameter setting (Yujie et al. 2020)

Peak strength/MPa	Young's modulus/GPa	Poisson's ratio	Shear modulus/GPa	Bulk modulus/GPa	Tensile strength/MPa
137.7	54.6	0.27	13.56	24.96	9.55

Where Q, F, B represent quartz, feldspar, biotite respectively. "in" denotes the contact parameters of intra-grains and "out" denotes the contact parameters of inter-grain.

Solving the thermal problem requires reconstructing the stress–strain equation, which requires subtracting the strain portion due to heat from the total strain. Thermal expansion does not contribute to angular variation in isotropic materials, so thermal expansion does not affect the shear strain increment. The incremental thermal strain is related to the coefficient of thermal expansion, which gives the equation:

$$\Delta\epsilon_{ij} = \alpha_t \Delta T \delta_{ij} \tag{1}$$

where α_t denote coefficient of thermal expansion; ΔT denote temperature difference variation; δ_{ij} denote the Kronecker factor.

From the above calculation of strain, the thermal stress coupling calculation can be obtained (Itasca Consulting Group 2019):

$$\Delta\sigma_{ij} = -3K\alpha_t \Delta T \delta_{ij} \tag{2}$$

where K denotes bulk modulus,

Table 3 The contact parameters used for the simulations in this paper

Name	Jkn (GPa)	Jks (GPa)	Friction (°)	Friction residual (°)	Cohesion (MPa)	Tensile (MPa)
CtQ-Qin	21,900	16,500	45	5	48	21.3
CtQ-Qout	14,600	11,000	45	5	32	14.2
CtQ-F	17,200	9460	39	5	42.5	15.35
CtQ-B	140,300	35,500	49	5	25.5	15.9
CtF-Fin	29,700	11,880	33	5	79.5	24.75
CtF-Fout	19,800	7920	33	5	53	16.5
CtF-B	142,900	33,960	43	5	36	17.05
CtB-Bin	399,000	90,000	53	5	28.5	26.4
CtB-Bout	266,000	60,000	53	5	19	17.6

3DEC allows only one-way thermal coupling to occur. Temperature changes can cause thermal strain and, thus, thermal stress.

3 Thermal conditions and evaluation of thermal damage

3.1 Three distinct thermal conditions

In this study, the temperature distribution, maximum principal stress distribution, and displacement distribution are examined for three different thermal conditions. The joint plane normal displacement is specifically analyzed as it provides a better representation of cracks in the rock model.

The simulation process involves gradually heating the model from the outside. Rapid heating entails reaching a temperature of 600 °C according to a specific temperature gradient and maintaining a constant temperature load of 600 °C outside the model until the entire model reaches 600 °C. On the other hand, slow heating starts from an initial room temperature of 25 °C and gradually heats the exterior of the model to 100 °C. This temperature is maintained until all parts of the model reach 100 °C. This process is repeated in intervals of 100 °C until the entire model is heated to 600 °C. Slow heating allows for a longer heating time, resulting in more uniform heating of the model and a smaller real-time temperature gradient within the model compared to rapid heating.

Cyclic heating is similar to rapid heating conditions, initially heating the model from 25 to 200 °C. However, after reaching 200 °C, a low-temperature load of 25 °C is applied directly to the model's exterior until the temperature of the entire model is reduced back to 25 °C. The model is then heated again in a sequential cycle, similar to the first heating process. The heating temperature gradients remain consistent across all thermal conditions. It should be noted that under slow and cyclic heating conditions, the author observed certain units that did not reach uniform temperatures, referred to as "strange units" in this study. Each thermal condition requires a significant amount of time to reach thermal equilibrium, and for ease of calculation and description, every 50 million steps are denoted as a stage.

3.2 Rapid heating condition

The temperature distribution during rapid heating is illustrated in Fig. 7, revealing a smooth heating process without any visible cracks. Heat is transferred from the outside of the model, resulting in distinct isothermal ranges within the model. In the upper part of the model, a small region of slower heat transfer is observed at each stage.

Figure 8 displays the displacement distribution during rapid heating. The displacement magnitude gradually increases from the outer region towards the interior, with the external displacement consistently exhibiting the highest values. However, it is noteworthy that the central part of the model displays significantly smaller displacements compared to the surrounding areas, with values remaining within the range of less than 0.2 mm.

Figure 9 depicts the quarter section of the model, showcasing the maximum principal stress distribution on the outer surface. Observing the model's interior, it can be seen that the maximum principal stress experiences rapid growth. Conversely, the outer surface of the model undergoes a slower stress development. In the upper part of the outer surface, the maximum principal stress transitions from a negative value to disappearance within a small grain, eventually reaching its maximum at stage 6. Upon reaching thermal stability, no compressed grains are present on the surface. In contrast, the corresponding inner part of the model exhibits specific compressed maximum principal stress values during the final stage. During the data analysis, the author observed a sudden change in the color of some adjacent blocks in the figure, after setting a fixed numerical scale. This occurrence can be attributed to the consideration of maintaining consistency in the legend, which resulted in a slight distortion in the color representation throughout the entire simulation process. It is important to highlight that the variation in the distribution of maximum principal stress is also influenced by the diverse mechanical properties of different minerals, such as thermal expansion coefficient and elastic modulus. These variations can potentially impact the occurrence of internal and external cracking in the rock. The limitations of the DEM calculation method may result in the obstruction of force and temperature transfer due to block deformation, contact failure,

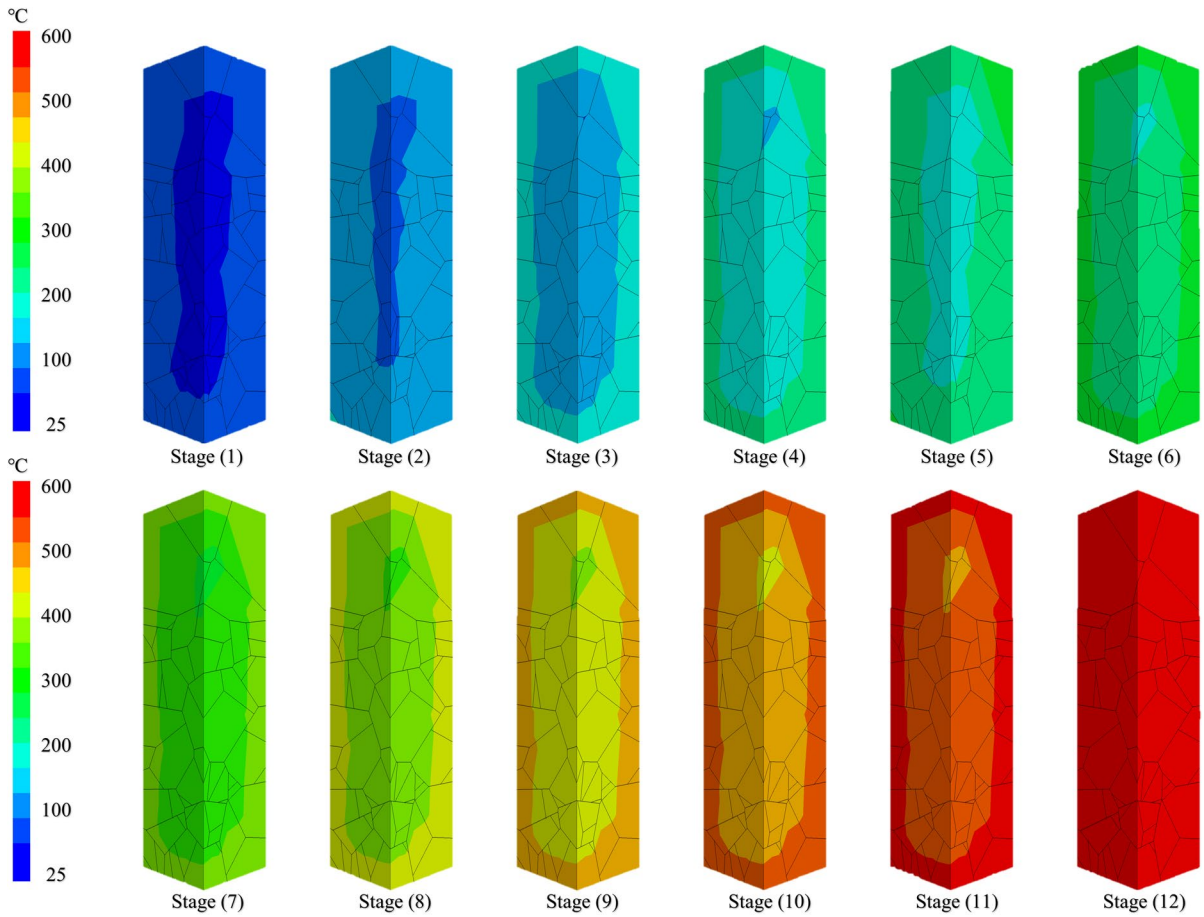

Fig. 7 Rapid heating temperature distribution

or local subcontact failure. A similar situation is observed in the following figures, such as Figs. 13 and 19. In comparison to the temperature distribution and displacement distribution, the sudden change in the distribution of the maximum principal stress is attributed to the calculation of the maximum principal stress using formulas, which amplifies the non-uniformity of the internal structure of the model.

Uniaxial compression simulations were conducted to examine the thermo-mechanical coupling stages of the model. Figure 10 presents representative stress–strain curves obtained from the uniaxial compression tests at different stages. The peak compressive strength and the magnitude of the elastic modulus were determined for each stage. The stress–strain diagram in Fig. 10a reveals a notable decrease in both peak stress strength and elastic modulus during the heating simulation. Moreover, the residual strength of the uniaxial compression test also exhibited a significant reduction, with the final heating stage showing a residual strength of only about 10 MPa. Notably, as the temperature exceeded 500 °C during the heating process, a more pronounced ductile transition was observed in the model, resulting in a broader peak segment in the stress–strain curve. Figure 10b illustrates the peak strength and Young's modulus curves obtained using the Gaussian fitting method. The curves exhibit a gradual decrease with increasing temperature and possess a concave shape. The rate of decrease diminishes gradually with temperature, eventually approaching stability. In numerical terms, both indicators decrease by nearly 50%. These mechanical parameters provide evidence of severe rock damage, yet the rock retains some residual strength at the end of the process.

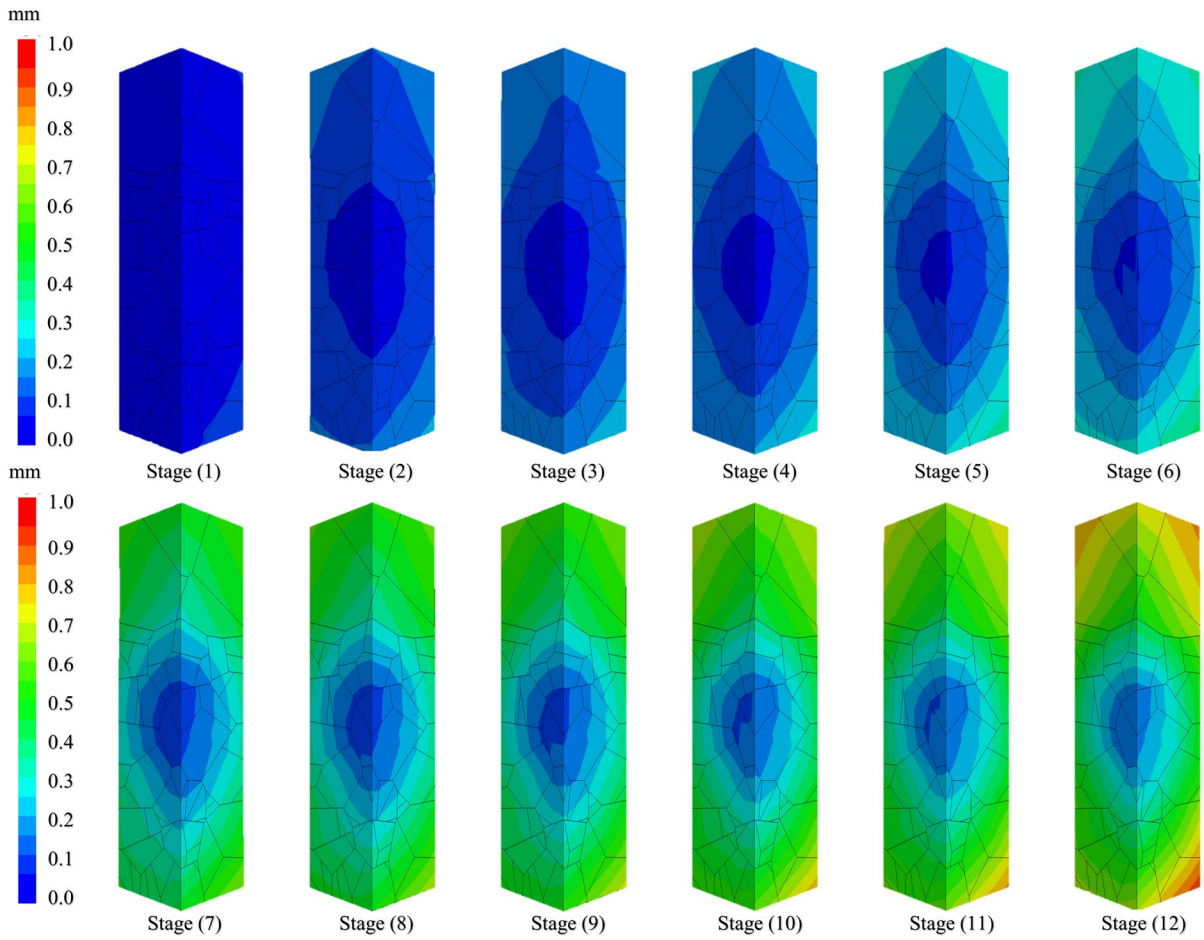

Fig. 8 Rapid heating displacement distribution

3.3 Slow heating condition

Figure 11 illustrates the temperature distribution of the rock under slow heating, ranging from 100 to 600 °C, displayed from left to right and top to bottom. For temperatures between 100 and 500 °C, a similar heating trend can be observed, displaying certain patterns. Notably, the proportion of low-temperature regions in Stage 5 decreases, indicating easier heat transfer. However, when examining the heating from 500 to 600 °C, a peculiar phenomenon becomes apparent from Stage 4 onwards in the temperature distribution of the model's blocks. This phenomenon becomes more pronounced in Stage 5, and by Stage 6, one block is still seen not reaching 600 °C. The occurrence of significant fractures during the 500–600 °C process disrupts the temperature transfer process, leading to this anomalous behavior. This conclusion is further supported by the stress–strain curves of the uniaxial compression tests, providing a visual confirmation.

Figure 12 presents the displacement distribution of the slowly heated model. It can be observed that the displacement remains close to zero at 100 °C and 200 °C. The displacement gradually increases at a slow pace at 300 °C, 400 °C, and 500 °C. However, at 600 °C, there is a sudden change in displacement during the last two stages, with external displacement increasing rapidly while internal displacement increases more slowly. This behavior aligns with the peculiar temperature distribution phenomenon observed earlier.

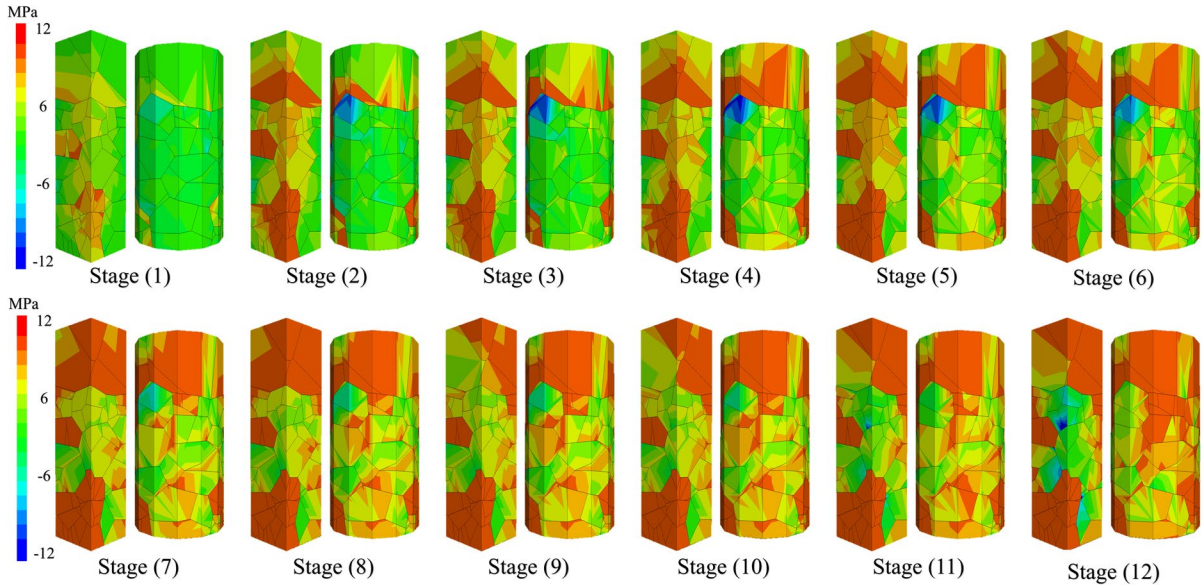

Fig. 9 Maximum principal stress of rapid heating

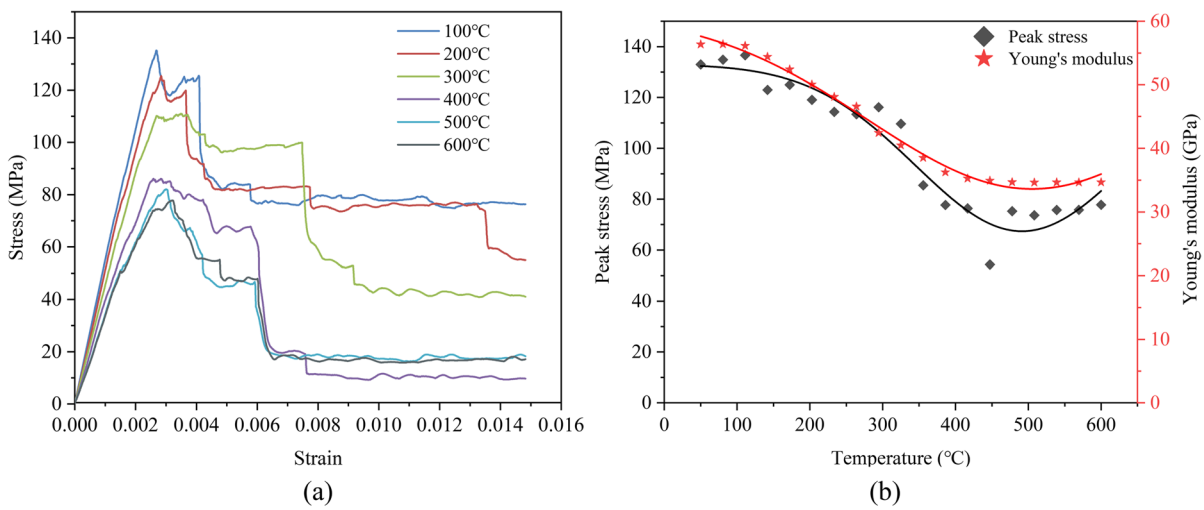

Fig. 10 UCS on models after rapid heating **a** Stress–strain curve under rapid heating condition; **b** Curves of peak stress and Young's modulus with temperature for the model under rapid heating condition

Figure 13 demonstrates the maximum principal stress field during slow heating. The model undergoes a rapid change in the stress field internally. In the last heating stage, cracks are clearly visible on the model's surface in the final two plots. Comparing the stress field diagrams inside the model, these cracks may be attributed to negative internal stresses. Notably, no visible cracks are observed internally. Throughout the slow heating process to 600 °C, consisting of six large heating stages, the stress field changes inside the model precede the surface changes. Some stages exhibit a more prominent negative maximum principal stress in the upper part of the internal stress field, indicating the squeezing of certain grains.

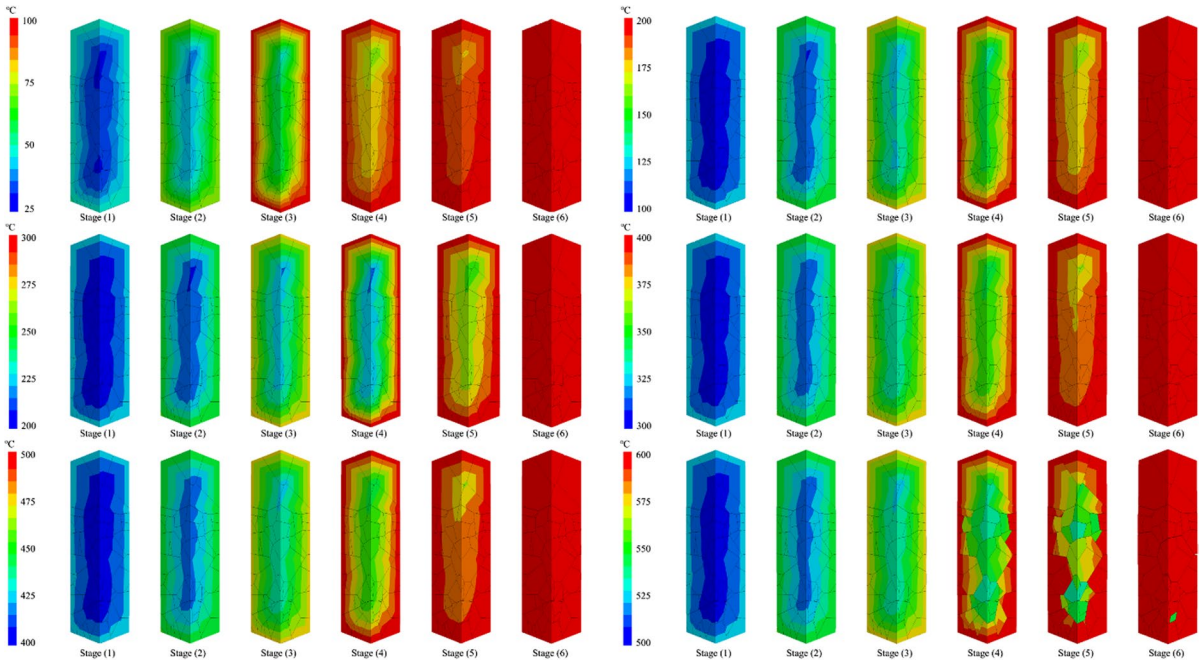

Fig. 11 Slow heating thermal distribution

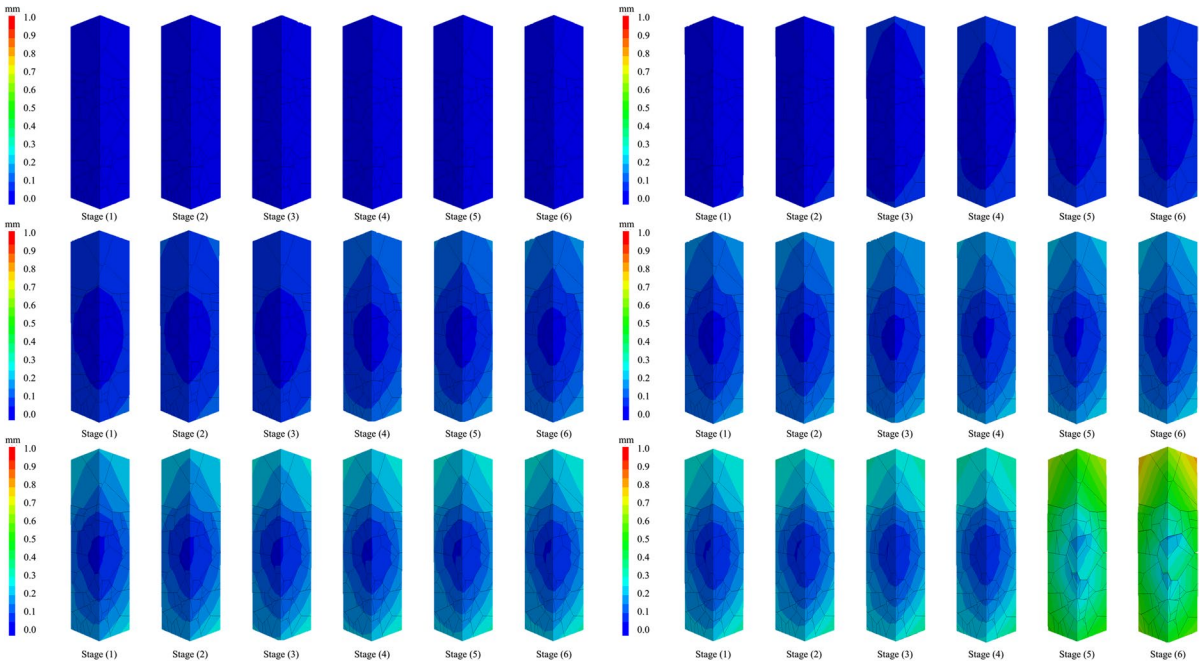

Fig. 12 Slow heating displacement distribution

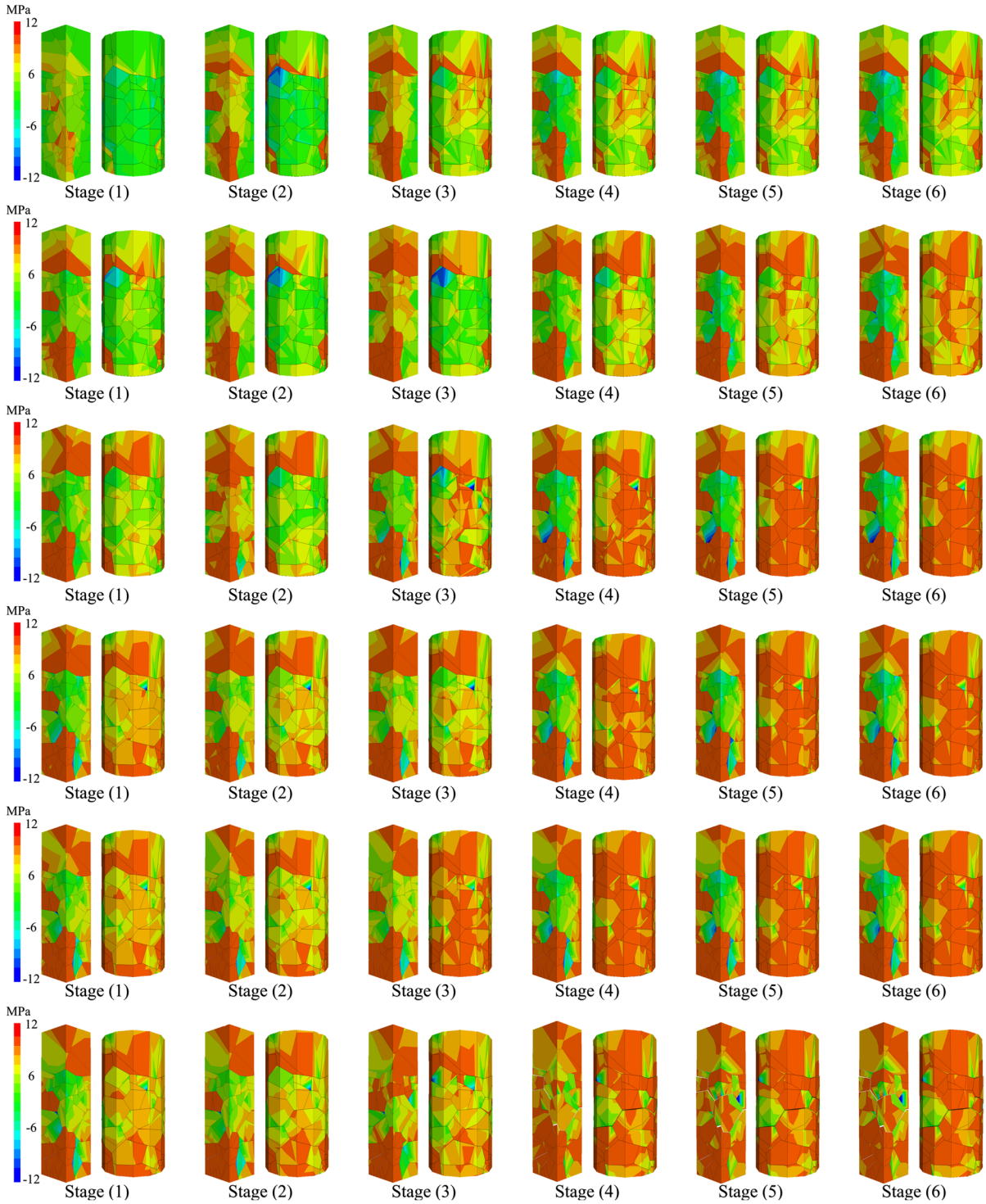

Fig. 13 Slow heating maximum principal stress

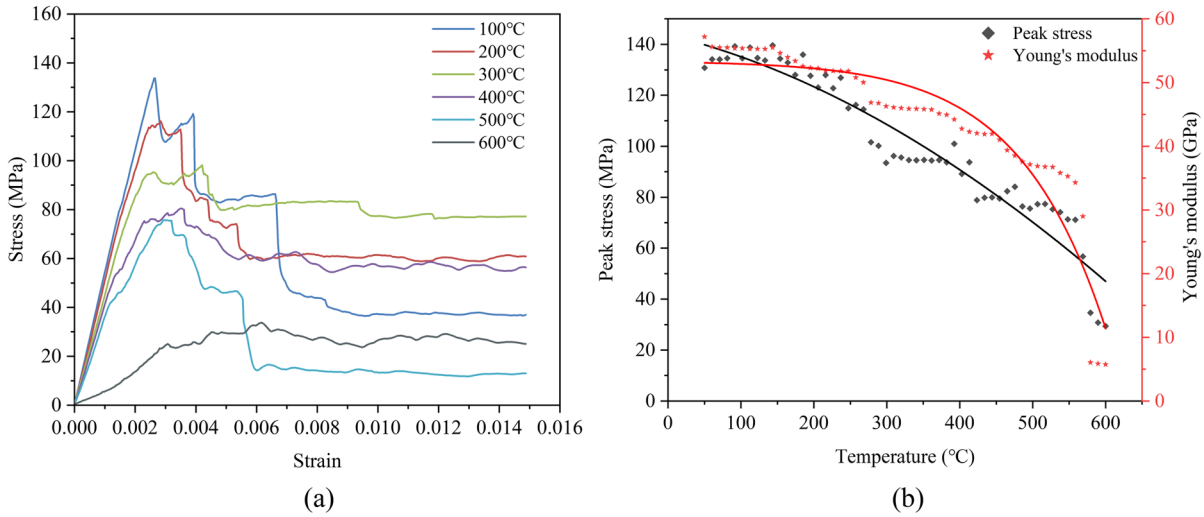

Fig. 14 UCS on models after slow heating **a** Stress–strain curve under slow heating condition; **b** Curves of peak stress and Young's modulus with temperature for the model under slow heating condition

The stress–strain curves for each stage under slow heating conditions are presented in Fig. 14a. Similar to the rapid heating scenario, the peak stress strength of the uniaxial compression tests gradually decreases, and the elastic modulus also exhibits a decreasing trend. However, there are notable differences when comparing the residual strengths after the peak. The residual strength at 100 °C is significantly lower than that at 200 °C and 300 °C. The residual strength at 200 °C and 400 °C is nearly identical, while the residual strength at 300 °C is considerably higher than that at 200 °C and 100 °C. Examining the stress–strain curves, the latter stages show an increasing resemblance to ductile stress–strain curves. The figure illustrates that the peak strength is associated with a larger strain and a higher proportion of residual compressive strength after the peak. The descending section after the peak indicates a gradual transition in failure mode from unheated brittle failure to ductile failure. The six curves demonstrate a gradual decrease in peak strength and elasticity during the slow heating process, accompanied by a process of damage accumulation. At a temperature of 600 °C, the stress and strain undergo ductile changes, resulting in a peak strength lower than 40 Mpa and a reduction of more than half in Young's modulus. This confirms the transition from brittleness to ductility.

Figure 14b presents the peak strength values and Young's modulus values obtained from a series of uniaxial compression tests, along with two curves generated by Gaussian fitting. In contrast to the previous rapid heating, the slow heating process undergoes multiple stages. Although the combined curve effect is not as ideal as rapid heating, it still reflects the overall trend of the entire process. Both curves demonstrate an upward convex shape, with the Young's modulus curve exhibiting slightly more pronounced behavior. The peak strength response demonstrates a relatively stronger correlation with temperature compared to Young's modulus. Towards the end of the heating process, both curves display a substantial decrease, indicating rapid deterioration. The later stages of heating are characterized by the development of numerous cracks, leading to a significant decrease in both peak stress and Young's modulus. At the conclusion of heating, both the peak stress and Young's modulus reach very low values, indicating a complete loss of strength and severe damage to the rock, accompanied by significant fractures.

3.4 Cycle heating condition

Figure 15 presents the temperature distribution of the rock under cyclic heating conditions. The first

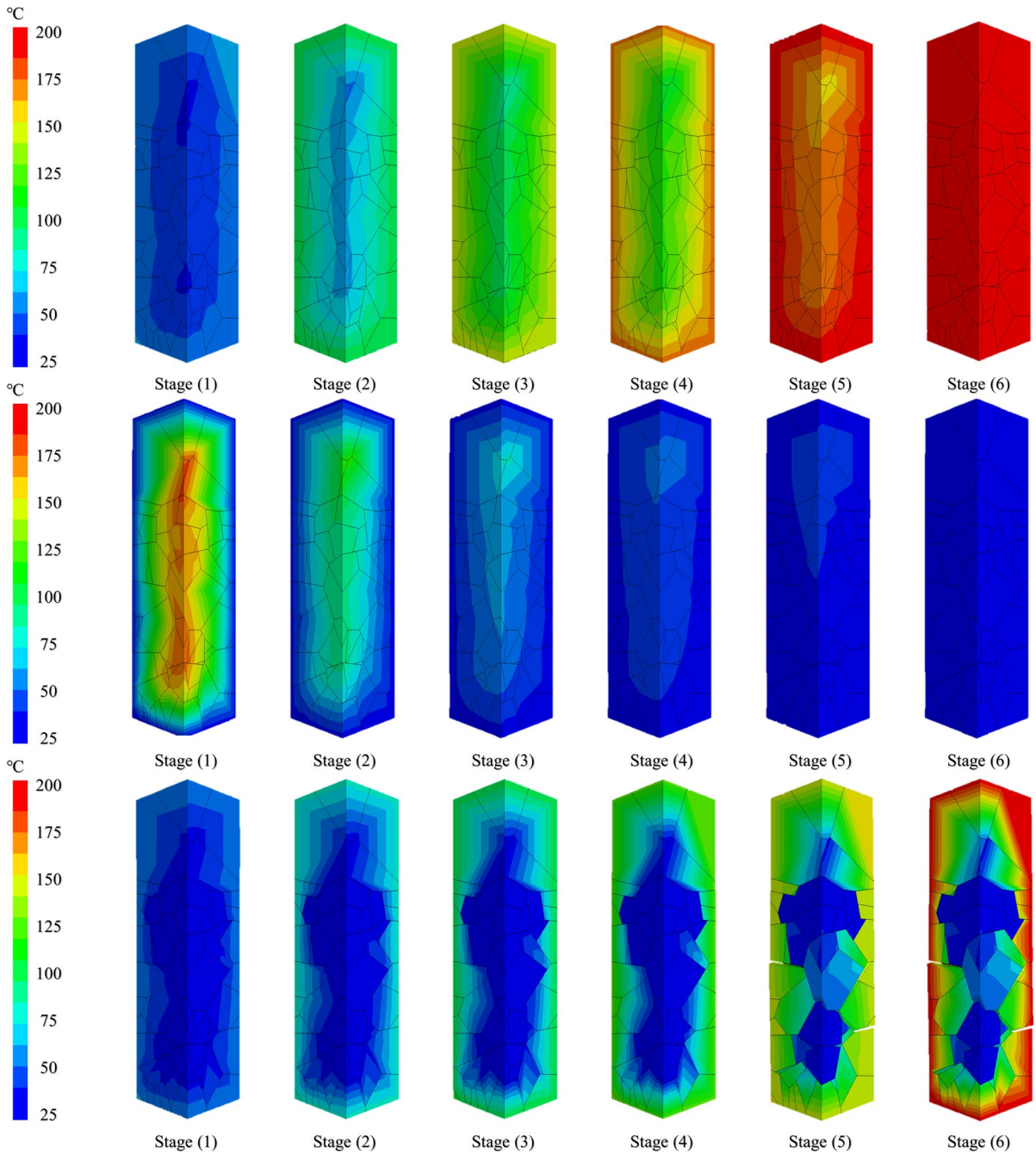

Fig. 15 Cycle heating thermal distribution

heating, cooling, and subsequent heating follow similar patterns as observed in the previous two working conditions. However, the phenomenon of blocked heat transfer becomes more pronounced during the second heating and occurs more rapidly. This trend becomes evident early in the heating process. In Stage 6, for instance, the external temperature reaches 200 °C, while the internal temperature remains below 50 °C. Notably, apparent cracks are observed in the model during Stages 5 and 6.

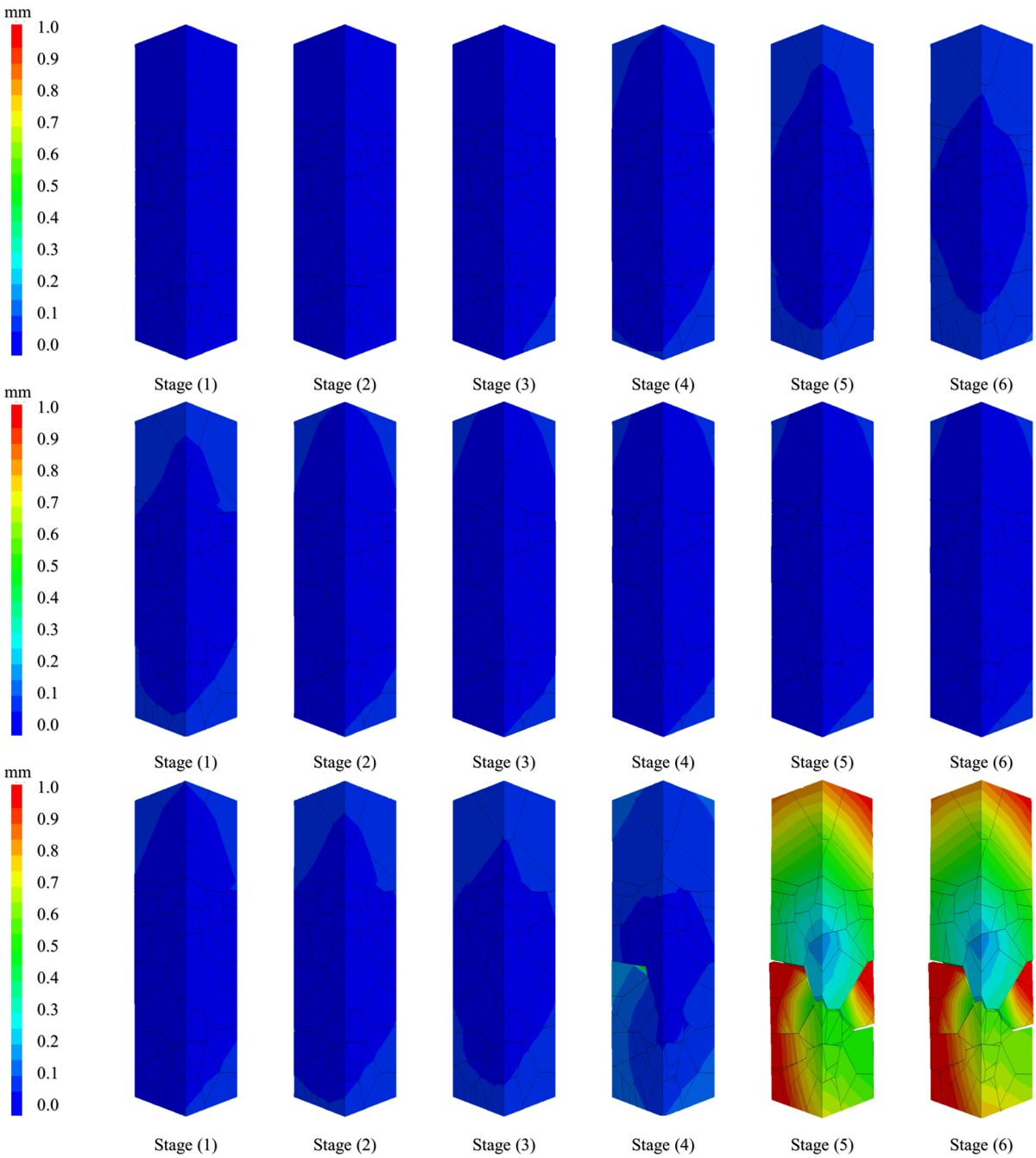

Fig. 16 Cycle heating displacement distribution

The displacement distribution for cyclic heating is illustrated in Fig. 16. During heating and cooling, no significant changes in displacement occur. However, during the second heating, an increase in the displacement distribution can be observed from Stage 4 onwards, originating from the interior of the model. Stages 5 and 6 exhibit larger displacements, attributed to the presence of crossing cracks.

Figure 17 showcases the maximum principal stress field during cyclic heating. Due to the addition of the

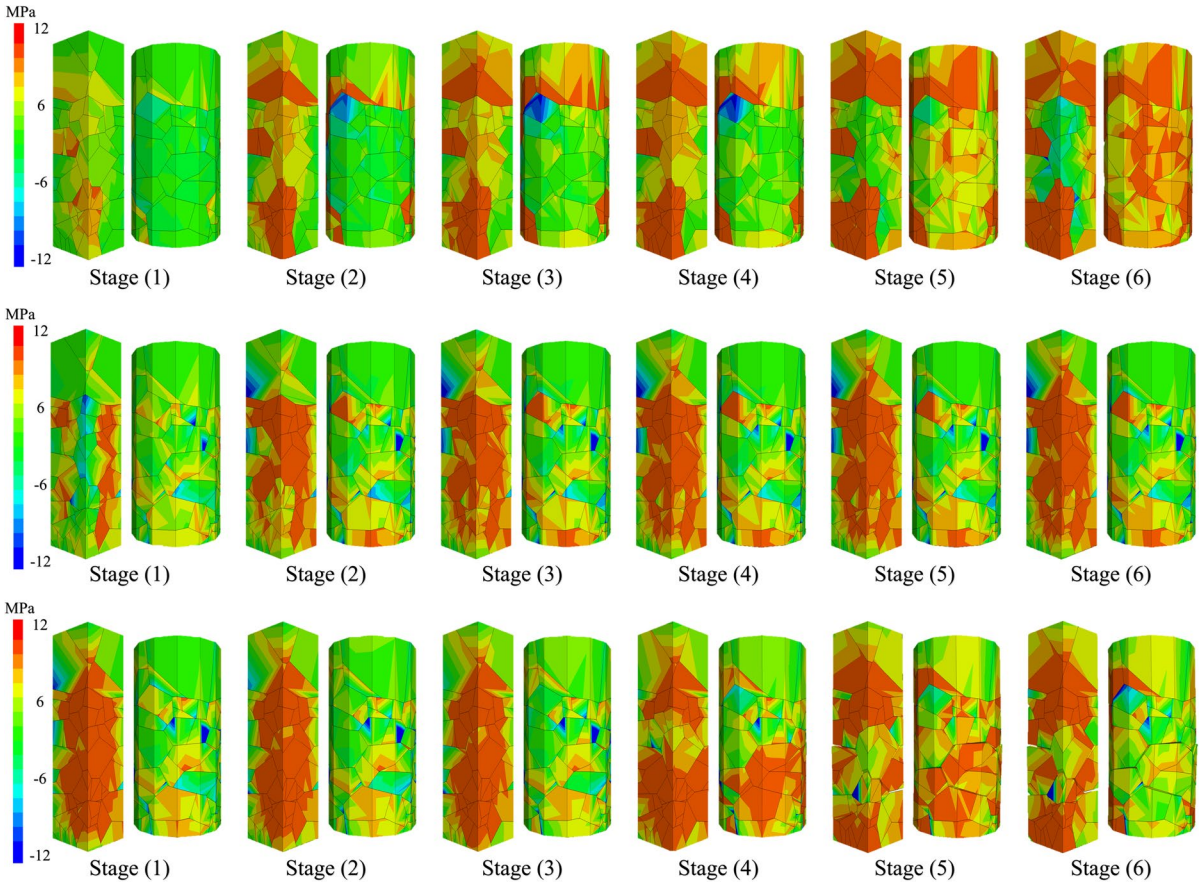

Fig. 17 Maximum principal stress of cycle heating

cooling process in the cyclic heating cycle, the distribution of maximum principal stress exhibits different phenomena and patterns. During the first heating process, a similarity to the previous two working conditions is observed, with focus given to the law of the maximum principal stress field inside the model during the cooling stage in comparison to the first stage. Comparing Stage 6 with the heating process, it is evident that the internal stress within the model during heating is close to zero, while the surface stress is more significant. Conversely, during the cooling process, the model exhibits larger internal stress and smaller surface stress, resulting in tensile stress on the surface and leading to crack formation during the second heating. Notably, in Stage 5 and Stage 6, prominent cracks appear, and stress is released at the crack locations. The internal principal stress field remains significant in particles that are not cracked, while the maximum principal stress near the cracks reduces to approximately zero. Furthermore, noticeable cracks are observed on the model's surface and within the model, indicating intra-grain damage throughout the entire model, which distinguishes it from the previous slowly heated working condition.

The stress–strain curve for cyclic heating is shown in Fig. 18a, from which it can be seen that the stress–strain curve for the final heating to 200 °C loses strength completely, with a stress maximum of only about 40 MPa. The strain curve shows that the model exhibits brittle failure characteristics during the initial heating and cooling stages. However, during the second heating process up to 200°, a clear ductile stress–strain curve emerges, accompanied by a noticeable decrease in Young's modulus.

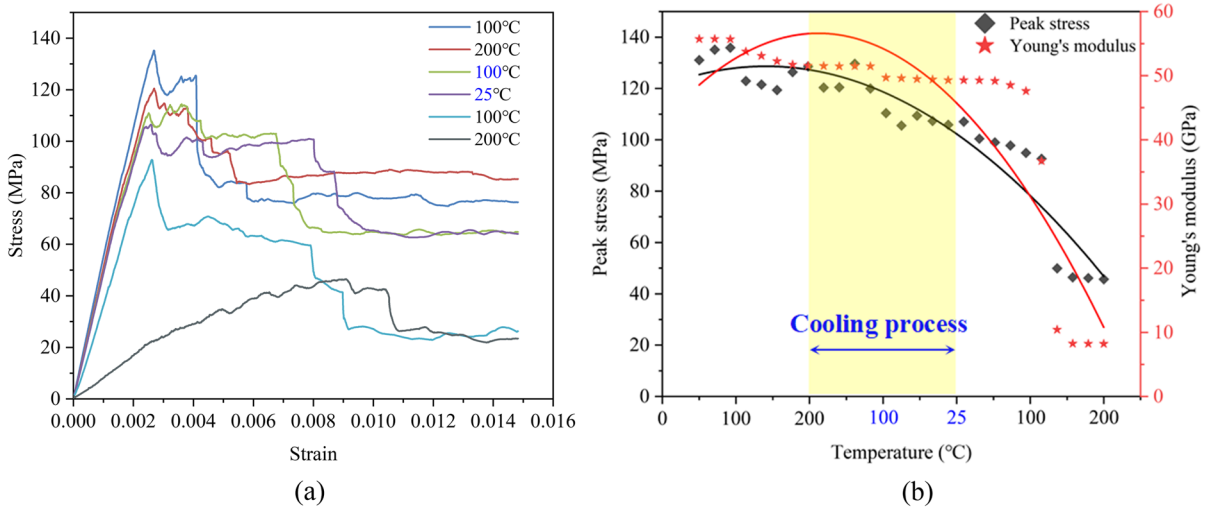

Fig. 18 UCS on models after cycle heating **a** Stress–strain curve under cycle heating condition; **b** Curves of peak stress and Young's modulus with temperature for the model under cycle heating condition

Figure 18b presents the two curves resulting from Gaussian fitting of the peak strength values and Young's modulus values obtained from a series of uniaxial compression tests. The fitting effect in this case is not as satisfactory as the first two cases, with some fluctuations observed at certain stages. Although the Young's modulus appeared to exhibit an upward trend, it should be noted that this change was not reflected in the data obtained. Both curves exhibit a convex upward shape. Notably, the sudden decrease in peak intensity and Young's modulus at the end of the heating phase causes some curves to exceed the actual values obtained during the fitting process. Throughout most of the time period, both curves show minimal changes. The author has used light yellow to distinguish the cooling process in the image. Following the initial heating stage, the volume of the block expands, leading to local tension or shear failure due to the varying thermal expansion coefficients between the blocks. This, in turn, results in local subcontact failure and the accumulation of damage, leading to a reduction in strength. During the cooling stage, a reverse process to the heating stage occurs, also causing local subcontact failure. After the accumulation of damage during these two stages, the second heating stage exhibits a rapid decrease in peak strength and Young's modulus due to the accumulated damage to cracks.

4 Discussion

4.1 Cracking behavior under varied heating conditions

Figure 19 illustrates the distribution of joint normal displacements of the entire model under three different heating conditions. In the figure, the joint surfaces with joint normal displacements greater than 0.1 mm are highlighted. The intensity of the red color represents the size of the displacements, with darker shades indicating wider cracks. For the rapid heating condition, as shown in Fig. 19a only one small and relatively continuous crack with narrow width was observed in the joint plane normal displacement diagram. The local magnification diagram of the grains showed almost no cracks.

In the case of slow heating, as shown in Fig. 19b, cracks were predominantly concentrated in the middle and upper part of the model. Combining Figs. 20 and 21, the magnification map of the minerals demonstrated intra-grain failure in enlarged biotite minerals and inter-grain failure in certain blocks, which is consistent with the original design purpose of the study.

Under the cycle heating condition as shown in Fig. 19c, the joint plane normal displacement

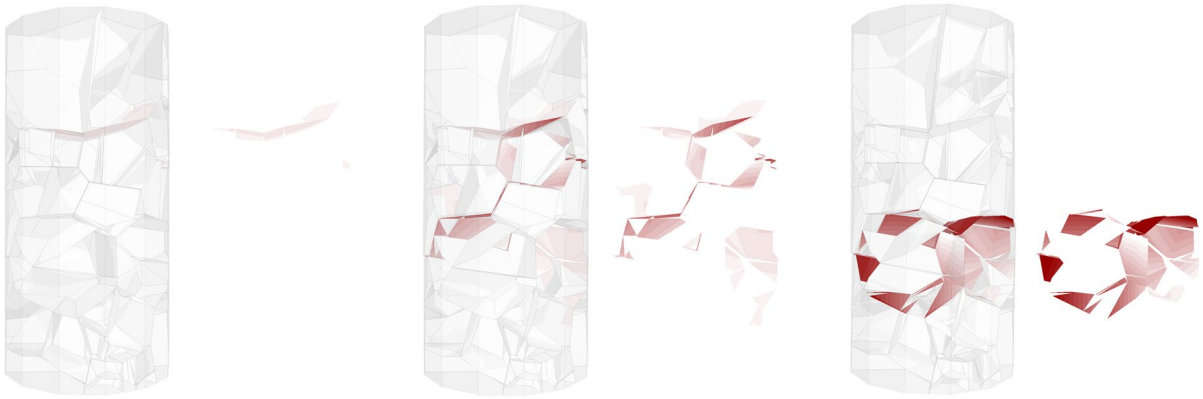

Fig. 19 Normal displacement of the three thermal conditions: **a** rapid heating condition; **b** slow heating condition; **c** cycle heating condition

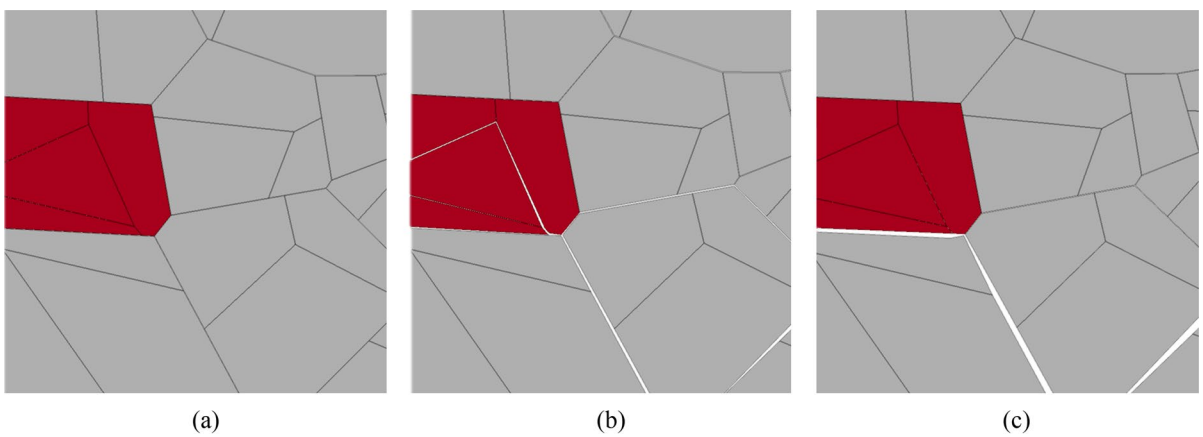

Fig. 20 Separate mineral amplification for the three thermal conditions: **a** rapid heating condition; **b** slow heating condition; **c** cycle heating condition

diagram showed that the damaged areas of the model were located in the central lower position, exhibiting more severe cracking compared to the other two thermal conditions. Millimeter-scale cracks were observed. In the local magnification of the minerals, significant inter-grain failure was observed, but intra-grain failure, which occurred during the cycle heating process, was absent. This phenomenon may be attributed to the introduction of the cooling process during the cycle heating, where the rock experienced both cold-brittle and hot-ductile behavior. Consequently, weaker contacts between grains failed first, releasing localized stresses and preventing failure within the grains. These findings highlight a significant distinction between these two situations.

4.2 Comparative analysis of thermal damage

Considering the temperature distribution, it can be concluded that rapid heating eventually achieves temperature stability in the temperature distribution. In contrast, the slow heating condition eventually shows some strange grains, and the cycle heating process shows strange grains earlier in the heating process.

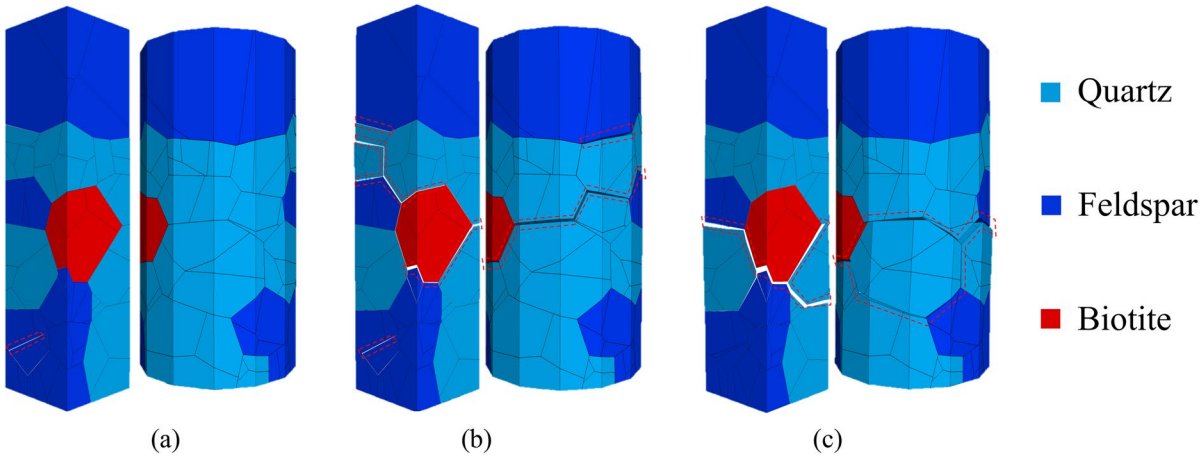

Fig. 21 Model mineral distribution diagram: **a** rapid heating condition; **b** slow heating condition; **c** cycle heating condition

The study comprehensively considers the temperature distribution, displacement distribution, and maximum principal stress distribution under three heating conditions. When comparing the displacement distribution, it is observed that the slow heating displacement distribution changes gradually until the end, where a more significant displacement change occurs. In contrast, rapid heating showed displacement changes of the same magnitude as slow heating after 300 °C, and by the end of heating, the displacement distribution was much larger than that of rapid heating. On the other hand, cycle heating shows a rapid displacement increase during the second heating period. Considering the stress field and the joint plane normal displacement, the rapid heating has only one smaller crack in the middle and upper part. Cracks were evident and more widely distributed in the slow heating condition. The number of cracks for cycle heating is less than for slow heating, but the extent of cracks is more significant than that for slow heating. Comparing the stress–strain curves, the decay of the final state stress–strain curves for slow heating and cycle heating is more obvious, which means that the model is more severely damaged. According to the modulus of elasticity and peak strength curves, the slow heating and cycle heating show a sudden decline at the end, and the cycle heating decreases more rapidly. In contrast, the rapid heating did not present such a change and still maintained the peak strength and modulus of elasticity at the end. For these phenomena, the reason is that the heating rate leads to a difference in the damage pattern, with slow heating having a longer heating time and the cooling process in cycle heating being the exact opposite of the heating process.

Regarding inter-particle damage and intra-particle damage, the author conducted a local comparative study using the same unit, as shown in Fig. 20. The figure distinguishes between red and gray. Figure 20a illustrates the damage of this unit under rapid heating, where almost no damage occurs. Figure 20b shows the damage of this unit under slow heating, revealing noticeable internal particle damage and circumferential damage. Figure 20c displays the damage of this unit under cyclic heating, indicating significant circumferential damage but no apparent internal damage. These findings in Fig. 20 confirm the variation in particle damage under different heating conditions. It is important to note that this variation is influenced by factors such as the non-uniformity of the model, thermophysical parameters, mechanical parameters between particles, and the local temperature gradient of the particles.

4.3 Impact of heterogeneity on crack propagation

In contrast to the previous peak strength curves, the peak strength of slow heating decreases more slowly while cycle heating decreases more sharply. The crack distribution of cycle heating appears to be cracked throughout the model, thus reflecting the fact that plastic deformation is greater in cycle heating than in slow heating conditions.

The analysis of specific minerals in the model is shown in Fig. 21. Light blue represents quartz minerals, dark blue represents feldspar minerals, and red represents biotite minerals. Figure 21a–c illustrate the final model results for rapid heating, slow heating, and cycle heating, respectively. It can be observed that Fig. 21a has almost no cracks, while both Fig. 21b and c show more noticeable cracks. Comparing Fig. 21b and c, it is evident that the crack extent is smaller under slow heating compared to cycle heating. Additionally, Fig. 21b has a higher number of cracks compared to Fig. 21c. Analyzing the cracked minerals and contacts, it can be observed that all the contact surfaces between biotite minerals and feldspar minerals in the model are cracked. On the other hand, the contact between biotite and quartz is not cracked in the upper half of the contact. Figure 21b shows that the contacts between the quartz minerals failed, while those in Fig. 21c did not. Granite is a fully crystalline plutonic rock. The overall strength of the model is primarily determined by the strength of the mineral particles (grains) and the strength of the interfaces between the minerals (contacts). The thermal expansion coefficients of quartz and mica minerals are significantly higher than those of feldspar minerals. When there is a temperature gradient within the particle, it can lead to damage in the model due to deformation inconsistencies. When quartz and mica minerals come into contact with feldspar minerals, the feldspar minerals are more likely to experience compression. Mica minerals, on the other hand, are prone to damage due to their low strength. As a result, the possibility of transgranular damage in mica minerals is higher compared to the other two minerals. It is important to note that the large particle size of the model used in this study causes the temperature to be transmitted initially to the outer surface of the block, creating a certain temperature stress within the block itself. This factor may influence the development of fractures.

This study mainly studies the cracking patterns of cracks and concludes, including the degree of cracking and the number of cracks that have a direct relationship with the heating mode. It can be concluded that the slow heating results in a higher number of cracks and a more widespread distribution of cracks inside and outside the model. However, including the cooling process directly at room temperature, the extent of cracks caused by cycle heating will be more serious, and the inside of the model will be completely peeled off. In terms of the cracking mechanism, the initiation of cracks by slow heating is due to the failure of the contact between local grains, which causes the initiation and development of cracks, while cycle heating is due to the internal thermal stress to raising a crack. On this basis, the rapid expansion causes the bonded contacts to be damaged by tension due to the development of cracks.

5 Conclusions

Two scales of configuration methods are used to simulate the rock cracking laws and mechanisms under different thermal conditions. The following conclusions are mainly derived.

(1) A discrete element numerical modeling method is proposed to respond accurately to the thermal fracture characteristics of granite under various thermal conditions. The method is based on two scales and integrates the grain-growth model with the geometric model of Voronoi polygon configuration, which fully considers the non-uniformity of granite and can simulate various contact types, including the internal and external of the particles. Consequently, the method can efficiently and accurately simulate the possible damage patterns of inter- and intra-grain failure of mineral grains. The intra-grain damage mainly occurs in the slow heating process, and the cycle heating is dominated by inter-grain failure.
(2) Under different thermal conditions, the thermal field of the rock is essentially a transfer of temperature from outside to inside, but as the simulation proceeds, the thermal field is hindered by the development of fissures, and partial unit insulation occurs. The displacement distribution is characterized by small internal and large external displacement and, in general, increases slowly as the external temperature rises, with a rapid increase occurring at the crack initiation stage.
(3) Comparing the mechanical properties of the thermal coupling and the damage evolution law under the three thermal conditions, in general, the mechanical responses of the three thermal conditions show a significant decrease in peak strength and modulus of elasticity, and the greater the

extent of cracking, the faster the decrease. It can be seen from the residual strength of slow heating that the process of slow heating also leads to a ductile shift in the residual strength after the rock peak. In addition to this, crack initiation under slow heating conditions can be considered as a result of the non-uniform distribution of local thermal stresses in the model making contact failure, while cycle heating is due to thermal stresses between mineral grains, which leads to overall failure due to rapid expansion of cracks.

Acknowledgements This work is supported by the National Natural Science Foundation of China (52090081 and 41831290), the independent research project of State key Laboratory of Hydroscience and Engineering (2022-KY-02).

Author contribution QM: Conceptualization, Investigation, Formal analysis, Data curation, Writing—original draft; XL: Project administration, Supervision, Writing—review and editing, Funding acquisition; Danqing Song: Writing—review, Conceptualization, Methodology, Validation; EW: Project administration, Supervision, Writing—review and editing, Funding acquisition; JZ: Writing—review and editing; WY: Writing—review; MW: Writing—review and editing.

Funding This work is supported by the National Natural Science Foundation of China (52090081 and 41831290), the independent research project of State key Laboratory of Hydroscience and Engineering (2022-KY-02).

Data availability The data used in this research is restricted and not publicly available due to legal or ethical constraints. Interested researchers may request access to the data by contacting the corresponding author and obtaining necessary permissions, subject to the applicable restrictions.

Declarations

Conflict of interest The authors declare that there is no conflict of interest associated with this research. They have no financial or personal relationships that could influence the objectivity or impartiality of the study. This ensures transparency and upholds the integrity of the research presented in this manuscript.

Ethical approval This research adheres to the highest ethical standards, ensuring originality of the work, data integrity, proper citations, and avoidance of untrue statements or personal attacks.

Consent for publication The authors confirm that all necessary consents have been obtained from individuals and institutions involved in this research. Participants' informed consent has been secured for the use of their data, images, or any other identifiable information. This ensures compliance with ethical standards and permits the publication of this research in academic journals or other publications.

References

Bérest P, Brouard B (2003) Safety of salt caverns used for underground storage: blow out; mechanical instability; seepage; cavern abandonment. Oil Gas Sci Technol Revue De L Institut Francais Du Petrole 58:361–384

Chen B, Shen B, Zhang S, Li Y, Jiang H (2022) 3D morphology and formation mechanism of fractures developed by true triaxial stress. Int J Mining Sci Technol 32(6):1273–1284. https://doi.org/10.1016/j.ijmst.2022.09.002

Du H, Song D, Chen Z, Guo Z (2020) Experimental study of the influence of structural planes on the mechanical properties of sandstone specimens under cyclic dynamic disturbance. Energy Sci Eng 8(11):4043–4063

Elmo D, Stead D, Eberhardt E, Vyazmensky A (2013) Applications of finite/discrete element modeling to rock engineering problems. Int J Geomech 13(5):565–580

Ersoy H, Kolaylı H, Karahan M, Harputlu Karahan H, Sünnetci MO (2019) Effect of thermal damage on mineralogical and strength properties of basic volcanic rocks exposed to high temperatures. Bull Eng Geol Env 78:1515–1525

Freire-Lista DM, Fort R, Varas-Muriel MJ (2016) Thermal stress-induced microcracking in building granite. Eng Geol 206:83–93

Frost HJ, Thompson CV (1996) Computer simulation of grain growth. Curr Opin Solid State Mater Sci 1(3):361–368

Gautam P, Dwivedi R, Kumar A, Kumar A, Verma A, Singh K, Singh T (2021) Damage characteristics of jalore granitic rocks after thermal cycling effect for nuclear waste repository. Rock Mech Rock Eng 54:235–254

Ghasemi S, Khamehchiyan M, Taheri A, Nikudel MR, Zalooli A (2020) Crack evolution in damage stress thresholds in

different minerals of granite rock. Rock Mech Rock Eng 53:1163–1178
Ghazvinian E, Diederichs M, Quey R (2014) 3D random Voronoi grain-based models for simulation of brittle rock damage and fabric-guided micro-fracturing. J Rock Mech Geotech Eng 6(6):506–521
Huang J, Liu X, Song D, Zhao J, Wang E, Zhang J (2022) Laboratory-scale investigation of response characteristics of liquid-filled rock joints with different joint inclinations under dynamic loading. J Rock Mech Geotech Eng 14(2):396–406
Itasca Consulting Group I (2019) Numerical thermal formulation. http://docs.itascacg.com/3dec700/3dec/docproject/source/options/thermal/thermal_numerical.html?node3345
Jing L, Stephansson O (2007) Fundamentals of discrete element methods for rock engineering: theory and applications. Elsevier
Johnson B, Gangi A, Handin J (1978) Thermal cracking of rock subjected to slow, uniform temperature changes. In: 19th US symposium on rock mechanics (USRMS)
Kochkin B, Malkovsky V, Yudintsev S, Petrov V, Ojovan M (2021) Problems and perspectives of borehole disposal of radioactive waste. Prog Nucl Energy 139:103867
Kumari W, Beaumont D, Ranjith P, Perera M, Avanthi Isaka B, Khandelwal M (2019) An experimental study on tensile characteristics of granite rocks exposed to different high-temperature treatments. Geomech Geophys Geo-Energy Geo-Resour 5:47–64
Lei R, Wang Y, Zhang L, Liu B, Long K, Luo P, Wang Y (2019) The evolution of sandstone microstructure and mechanical properties with thermal damage. Energy Sci Eng 7(6):3058
Li J, Kaunda RB, Arora S, Hartlieb P, Nelson PP (2019) Fully-coupled simulations of thermally-induced cracking in pegmatite due to microwave irradiation. J Rock Mech Geotech Eng 11(2):242–250
Li Z-W, Long M-C, Feng X-T, Zhang Y-J (2021) Thermal damage effect on the thermal conductivity inhomogeneity of granite. Int J Rock Mech Min Sci 138:104583
Li Y, Xie H, Dong C, Wang S, Wan Y (2022) Zircon evolution from migmatite to crustally-derived granite: a case study of late Neoarchean migmatite in the Yishan area, western Shandong, North China Craton. Gondwana Res 112:82–104
Luc Leroy MN, Marius FW, François N (2021) Experimental and theoretical investigations of hard rocks at high temperature: applications in civil engineering. Adv Civil Eng 2021:1–21
Qin Y, Tian H, Xu N-X, Chen Y (2020) Physical and mechanical properties of granite after high-temperature treatment. Rock Mech Rock Eng 53:305–322
Quey R, Renversade L (2018) Optimal polyhedral description of 3D polycrystals: method and application to statistical and synchrotron X-ray diffraction data. Comput Methods Appl Mech Eng 330:308–333
Quey R, Dawson P, Barbe F (2011) Large-scale 3D random polycrystals for the finite element method: generation, meshing and remeshing. Comput Methods Appl Mech Eng 200(17–20):1729–1745
Quey R, Villani A, Maurice C (2018) Nearly uniform sampling of crystal orientations. J Appl Crystallogr 51(4):1162–1173
Shang X, Zhang Z, Xu X, Liu T, Xing Y (2019) Mineral composition, pore structure, and mechanical characteristics of pyroxene granite exposed to heat treatments. Minerals 9(9):553
Srinivasan V, Tripathy A, Gupta T, Singh T (2020) An investigation on the influence of thermal damage on the physical, mechanical and acoustic behavior of Indian Gondwana shale. Rock Mech Rock Eng 53:2865–2885
Toifl M, Hartlieb P, Meisels R, Antretter T, Kuchar F (2017) Numerical study of the influence of irradiation parameters on the microwave-induced stresses in granite. Miner Eng 103:78–92
Tripathi A, Gupta N, Singh AK et al (2021) Effects of elevated temperatures on the microstructural, physico-mechanical and elastic properties of Barakar sandstone: a study from one of the world's largest underground coalmine fire region, Jharia, India. Rock Mech Rock Eng 54(3):1293–1314
Vogler D, Walsh SD, von Rohr PR, Saar MO (2020) Simulation of rock failure modes in thermal spallation drilling. Acta Geotech 15:2327–2340
Wang X, Cai M (2018) Modeling of brittle rock failure considering inter-and intra-grain contact failures. Comput Geotech 101:224–244
Wang X, Cai M (2019) A comprehensive parametric study of grain-based models for rock failure process simulation. Int J Rock Mech Min Sci 115:60–76
Wang F, Konietzky H (2020) Thermal damage evolution of granite under slow and high-speed heating conditions. Comput Geotech 123:103590
Wu Z, Zhou Y, Weng L, Liu Q, Xiao Y (2020) Investigation of thermal-induced damage in fractured rock mass by coupled FEM-DEM method. Comput Geosci 24:1833–1843
Yang Y, Zheng K, Li Z, Li Z, Si L, Hou S, Duan Y (2019) Experimental study on pore-fracture evolution law in the thermal damage process of coal. Int J Rock Mech Min Sci 116:13–24
Yujie Z, Xiaoli L, Enzhi W (2020) Influence of impoundment gravity and pore pressure on reactivation of faults. Geomech Geophys Geo-Energy Geo-Resour 6:1–19
Zhao D, Wu J, Li Z (2022) Simulation and experimental research on ultrasonic vibration high temperature rock. J Petrol Sci Eng 212:110255
Zuo JP, Wang J-T, Sun Y-J, Chen Y, Jiang G-H, Li Y-H (2017) Effects of thermal treatment on fracture characteristics of granite from Beishan, a possible high-level radioactive waste disposal site in China. Eng Fract Mech 182:425–437